

# Dual-Robot Ultrasound-Guided Needle Placement: Closing the Planning-Imaging-Action Loop

Risto Kojcev<sup>1,2</sup> · Bernhard Fuerst<sup>1,3</sup> ·  
Oliver Zettinig<sup>3</sup> · Javad Fotouhi<sup>1</sup> · Sing  
Chun Lee<sup>1</sup> · Russell Taylor<sup>4</sup> · Edoardo  
Sinibaldi<sup>2</sup> · Nassir Navab<sup>1,3</sup>

Received: date / Accepted: date

**Abstract** *Purpose:* Precise needle placement is an important task during several medical procedures. To inject the needle into soft tissue, ultrasound imaging is used to guide the needle towards the target region. This task remains challenging due to the user's dependence of ultrasound imaging, limited field of view, moving target and moving needle. In this paper we present a dual-robot framework for robotic needle insertions under robotic ultrasound guidance. This system allows robotic needle insertion to target a preoperatively defined region of interest, while enabling real-time visualization using robotic imaging, and adaptive trajectory planning to provide safe and quick interactions.

*Method:* The proposed solution integrates impedance-controlled ultrasound image acquisition, registration of preoperative and intraoperative images, visual servoing, target localization, and needle tracking.

*Results:* In a simulated needle biopsy procedure, the system is evaluated under realistic conditions in a mock operating room. The robot-to-robot calibration and tracking algorithms allow the accurate (targeting error around 1mm) and clinically relevant biopsy of a region of interest.

*Conclusion:* Experimental results show the feasibility, and demonstrate the accuracy and robustness of the process. This shows that we can close the loop of planning and execution of the needle placement.

## 1 INTRODUCTION

Several medical procedures require the targeted insertion of a needle to perform diagnosis or treatment. Commonly performed applications include the administration of drugs (e.g. nerve block, tumor treatment, etc.), brachytherapy, ablation, or

---

E-mail: risto.kojcev@iit.it; rkojcev1@jhu.edu

<sup>1</sup> Computer Aided Medical Procedures, Johns Hopkins University, Baltimore, MD, United States

<sup>2</sup> Center for Micro-BioRobotics, Istituto Italiano di Tecnologia, Pontedera (PI) Italy

<sup>3</sup> Computer Aided Medical Procedures, Technische Universität München, Munich, Germany

<sup>4</sup> Laboratory of Computational Sensing and Robotics, Johns Hopkins University, Baltimore, MD, United States

biopsies of cysts, lymph nodes or lesions [1]. For many interventions, the outcome of the procedure is tightly correlated to the targeted accuracy of the needle tip placement, which highly depends on the analytical skills as well as the dexterity of the medical expert. Robot-assisted needle insertion may overcome user dependencies and yield a higher average anatomical targeting accuracy. While diagnosis and planning are frequently based on preoperative imaging, such as Computed Tomography (CT) or Magnetic Resonance Imaging (MRI), the procedures are often guided intraoperatively by ultrasound imaging. Although ultrasound image acquisition is strongly dependent on the operator, it is frequently used due to its non-invasive nature, low cost and high frame rate. However, difficulties in manual ultrasound imaging during needle insertions also arise from the varying pressure applied to the soft tissue, and the changing orientation relative to needle and target. A robot holding the ultrasound probe, applying constant pressure from a desired angle, and maintaining visibility of the needle in the ultrasound frame throughout the intervention, could facilitate various procedures currently requiring cumbersome eye-hand coordination.

In the past decade, research on ultrasound-guided robotic needle insertion has become of great interest to the scientific community. Using a fixed ultrasound transducer, a robotic needle insertion technique has been presented by Hong et al. [2]. That early work required the needle to be aligned with the ultrasound transducer, and the robotic component was designed to insert the needle along the ultrasound B-mode plane to target a region of interest in the image. Similar robotic needle insertion and steering concepts were presented for brachytherapy [3], soft tissue insertion [4], or obstacle avoidance [5]. While strongly focusing on the needle trajectory, the cited publications did not incorporate a moving (robotic) ultrasound acquisition. Therefore, they are limited by the field of view of the ultrasound transducer, and they possibly require a manual re-positioning.

To enable 3D needle steering, movement of the transducer may be required, as demonstrated in [6]. That proposed configuration is valuable and worked well for the performed experiments, but it may be difficult to apply the methodology in a clinical scenario due to the robot kinematics (linear stages might not be sufficient to cover patient motions realistically) and lack of force sensing.

While focusing on needle steering, the work presented in [7] used two robots: one inserting a needle, and a second one holding an ultrasound transducer. That work would theoretically support robotic ultrasound and re-positioning of the transducer to enable various needle trajectories. However, the cited work did not incorporate a moving transducer, and the method neither defines nor tracks the target anatomy. Nonetheless, it strongly motivates further research enabling robotic needle insertion and robotic imaging.

Finally, in [8], a system for calibration of 2D ultrasound images for 3D biopsies is presented. External optical trackers are used to estimate the pose of the hand-held needle relative to the robotically moved ultrasound probe. Because optical trackers are affected by the line-of-sight issue, the authors added additional infrared cameras to deal with occlusions. The cited work primarily deals with the calibration, and does not incorporate robotic needle placement or tracking of the needle and target in the ultrasound image. Moving beyond this approach, our novel system incorporates vision-based needle detection and target tracking.

In this paper, we present a system incorporating two light-weight robots i) to autonomously acquire ultrasound images with one arm and place the transducer

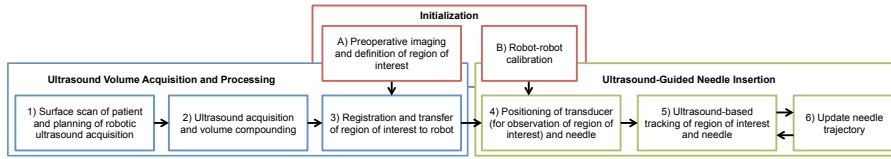


Fig. 1: The workflow is organized in three phases: the initialization phase (red boxes), ultrasound volume acquisition (blue boxes), and the ultrasound-guided needle insertion (green boxes). See section 2.1 for details.

so that ii) a needle can be inserted accurately with the other arm based on a preoperative definition of the region of interest and an intended needle target position. The flexible robotic image acquisition attempts to overcome limitations such as user-dependent ultrasound imaging quality or the necessity of a pre-defined configuration of patient and transducer, and does not require specialized 4D ultrasound transducers. In comparison to systems with a needle insertion guide or device attached to the ultrasound transducer [3], using a second robotic arm for the needle insertion retains the full versatility with respect to meaningful acoustic windows for imaging and anatomically possible needle insertion paths.

More specifically, we use 3D surface scanning, execute autonomous impedance-controlled ultrasound image acquisition, perform automatic registration of preoperative and intraoperative images, perform visual servoing using an impedance controller. Thus, the presented framework does not only close the planning-imaging-action loop by bridging from the planning of a target site to real-time imaging to automatic needle insertion, but also forms a servoing-based control loop involving both robotic arms. As the approach is capable of tracking not only the needle but also the anatomical target site (therefore allowing to cope with non-static targets), corrections of both the transducer- and the needle-holding robot are possible during the intervention. This work combines the advantages of previous approaches, namely the preoperative planning, the real-time tracking of the needle, and the trajectory update. All our techniques are efficiently implemented utilizing the Graphical Processing Unit, enabling to use the full image resolutions at high frame rates.

The methods are presented in section 2, with a system overview provided in section 2.1. First, we will explain the fast and accurate steps to calibrate the robots and cameras (2.2). Then, we explain every single component: acquisition of ultrasound images and volume compounding, registration of preoperative and intraoperative images (2.3), and, finally, the ultrasound-guided needle insertion (2.4).

## 2 MATERIALS and METHODS

### 2.1 System Overview

To achieve robotic ultrasound-guided needle insertion based on preoperative imaging, several tasks need to be performed, which can be organized into three phases:

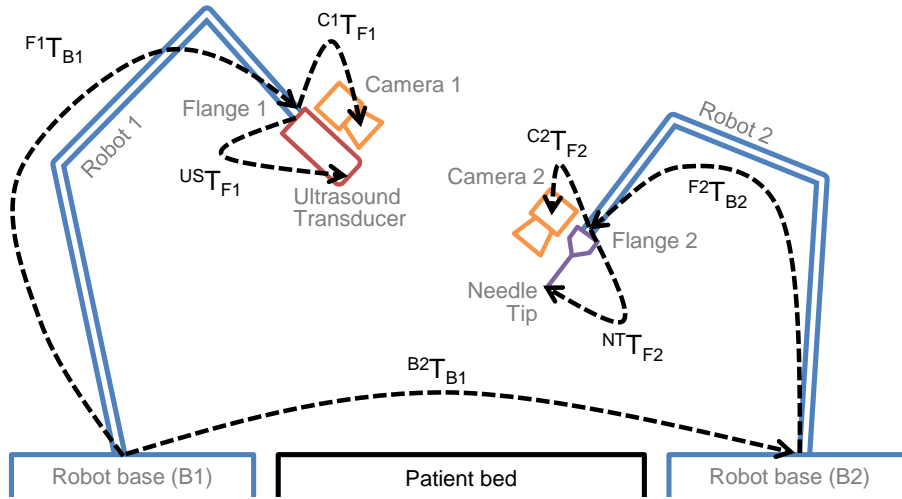


Fig. 2: The transformations base-to-flange  $F^{1,2}T_{B\{1,2\}}$ , flange-to-camera  $C^{\{1,2\}}T_{F\{1,2\}}$ , flange-to-needle tip  $NTT_{F2}$ , and base-to-base  $B^2T_{B1}$  need to be calibrated, while the transformations base-to-flange are provided by the robot.

initialization, ultrasound volume acquisition and processing, and ultrasound-guided needle insertion. The following paragraph refers to the workflow depicted in Fig. 1.

During the initialization phase (red boxes), medical experts review preoperative images and define the region of interest (A). The robot-robot calibration (B) is performed once the robots are definitively positioned in the intervention room, before the patient arrives. In the second phase, an autonomous ultrasound volume acquisition is performed using the first robot (blue boxes). This phase includes a 3D surface scan and planning of the ultrasound acquisition (1), ultrasound acquisition and volume compounding (2), and the registration of the preoperative images with the ultrasound volume (3). At this point, the region of interest is transferred to the robot coordinate system. In the third phase, the ultrasound-guided needle insertion is performed using the second robot (green boxes). Based on the ultrasound volume and preoperative imaging, the needle trajectory is planned. Then, the ultrasound transducer mounted on the first robot is positioned to enable the simultaneous observation of the needle and the region of interest (4). We define the ideal transducer position so that the needle moves within the imaging plane, as it is desired to observe the needle during the entire injection process. Following an automatic initialization of the needle position close to the point of entry to allow a final safety check, the second robot slowly inserts the rigid needle (5), and visual servoing allows the update of the needle trajectory based on the live ultrasound images and the tracked target anatomy and the needle tip is detected therein (6). The required steps for each of the three phases are explained in detail in the following sections.

## 2.2 Initialization: Robot and Camera Calibrations

In this section, we explain how to obtain the unknown transformations. Fig. 2 illustrates the chain of transformations in our dual robot setup, where each robot is equipped with a RGB-D camera, robot 1 holds the ultrasound transducer, and the needle is mounted on robot 2.

We use classical pivot calibration to compute the transformation flange-to-needle tip  ${}^{NT}\mathbf{T}_{F2}$  (see e.g. [9]). The transformations  ${}^{C\{1,2\}}\mathbf{T}_{F\{1,2\}}$  are obtained through hand-eye calibration [10], where  $\{1,2\}$  refers to robot 1 and 2. For one robot at two poses  $h$  and  $h+1$ , the chain of transformations can be defined as:

$${}^{C1_{h+1}}\mathbf{T}_{C1_h} {}^{C1}\mathbf{T}_{F1} = {}^{C1}\mathbf{T}_{F1} {}^{F1_{h+1}}\mathbf{T}_{F1_h}, \quad (1)$$

where the camera centers for pose  $h$  and  $h+1$  are obtained by tracking a checkerboard [11]. Finally, equation (1) needs to be solved for  ${}^{C1}\mathbf{T}_{F1}$ . The calibration for the second robot is performed analogously.

To perform ultrasound acquisition, the spatial transformation  ${}^{US}\mathbf{T}_{F1}$  from the origin of the ultrasound image to the transducer apex is defined as a combination of translation, rotation and scaling. The known design of the transducer mount is used to initialize the standard ultrasound-to-tracking calibration [12]. The Tool Center Points (TCP) are defined to be the ultrasound transducer apex and needle tip.

After flange-to-camera calibrations are performed for both robots, the base-to-base transformation  ${}^{B2}\mathbf{T}_{B1}$  is obtained by observing one common target, such as a checkerboard (CB):

$${}^{B2}\mathbf{T}_{B1} = {}^{F2}\mathbf{T}_{B2}^{-1} {}^{C2}\mathbf{T}_{F2}^{-1} {}^{CB}\mathbf{T}_{C2}^{-1} {}^{CB}\mathbf{T}_{C1} {}^{C1}\mathbf{T}_{F1} {}^{F1}\mathbf{T}_{B1}, \quad (2)$$

where  ${}^{CB}\mathbf{T}_{C\{1,2\}}$  are the transformations from camera center to checkerboard (CB) obtained as presented in [11]. To improve accuracy, the robot poses are varied, changing the transformations  ${}^{F\{1,2\}}\mathbf{T}_{B\{1,2\}}$  and  ${}^{CB}\mathbf{T}_{C\{1,2\}}$ , while observing the CB. The final base-to-base transformation  ${}^{B2}\mathbf{T}_{B1}$  is computed by averaging the base-to-base transformations computed at different robot poses. The calibration can easily be verified, by touching a common real world point or by aligning both flange end-effectors. It is assumed that during the procedure  ${}^{B2}\mathbf{T}_{B1}$  is not changed, therefore only one depth camera is used in the experimental setup.

To enable torque or impedance-controlled motion, the center of mass of each tool needs to be known. This can not be estimated based on the design of the mounts and tools, as the internal configuration of the cameras and the ultrasound transducer is proprietary. However, the load data can be determined using the internal torque sensors of the robot. During this procedure, the robot performs multiple measurements while several joints are moved. The load data and center of mass are computed based on these torque measurements [13].

## 2.3 Ultrasound Volume Acquisition and Processing

**3D Surface Scan:** To obtain a 3D scan of the patient's surface, one robot is manually positioned in an observation pose. Using the RGB-D camera mounted to the end-effector, the real-time RGB-D data is visualized and presented to the

operator for interactive selection by drawing a rectangle of the region of interest (ROI) containing the relevant part of the patient’s surface. To acquire useful ultrasound images of the selected ROI, the transducer needs to be placed perpendicular to the surface. Therefore, surface normal vectors are computed using a kNN-based approach [14].

**Trajectory Planning and Execution:** The planned trajectory is generated by projection of the ROI point cloud onto the frontal plane of the patient, building a 2D point cloud. The scan direction vector is identified by the first component of the principal component analysis (PCA). Before the ultrasound acquisition is executed, the operator is prompted to verify the sweep trajectory and that obstacles will be avoided. 2D ultrasound images are then recorded together with the mechanical tracking data provided by the robotic system. To achieve the acoustic coupling between ultrasound transducer and patient, the physician introduces ultrasound gel, and a dynamic behavior needs to be imposed to the interaction between robot end-effector and patient. During ultrasound acquisitions and needle insertion, the impedance control mode is used for achieving compliant robot behavior. Under impedance control the robot can react to influences such as obstacles or process forces. The motion model is based on virtual spring and dampers, which tensions vary based on currently measured and specified position of the TCP. Under impedance control it is possible to set the desired force that the robot exerts onto the patient’s surface, therefore enabling constant contact force between the ultrasound transducer and patient surface. The impedance controller is described in details in [13].

The growing stack of ultrasound images are visualized in real-time in 3D under consideration of the tracking data. This allows the physician to interrupt the acquisition at any time. After the data is recorded, the ultrasound volume is compounded using a quadrilateral interpolation for a good trade-off between computational performance and image quality [15].

**Registration of Preoperative and Intraoperative Imaging:** During the initialization phase, the physician selects the region of interest in preoperative images, such as Ultrasound, CT or MRI volumes. To obtain the position of this target in the robot coordinate system, the ultrasound and preoperative images need to be registered. The registration of images from different modalities is prone to fail when using common similarity measures, such as Sum of Squared Differences (SSD) or Normalized Cross-Correlation (NCC) [16]. Using the  $LC^2$  similarity measure [17, 18] and a non-linear optimizer, such as BOBYQA [19], the volumes can be aligned based on the intensity values and gradient information. In the current scenario, we expect the tissue deformation to primarily be caused by the pressure applied by the transducer. Therefore, we perform the registration by estimating an affine transformation to find the target within the ultrasound volume. After the confirmation by the operating physician, needle trajectory and new ultrasound transducer position are planned.

## 2.4 Ultrasound-Guided Needle Insertion

**Robot positioning and planning:** The needle injection point and trajectory are computed under the constraint that the ultrasound transducer is positioned perpendicular to the patient’s surface, and the needle and target appear on the

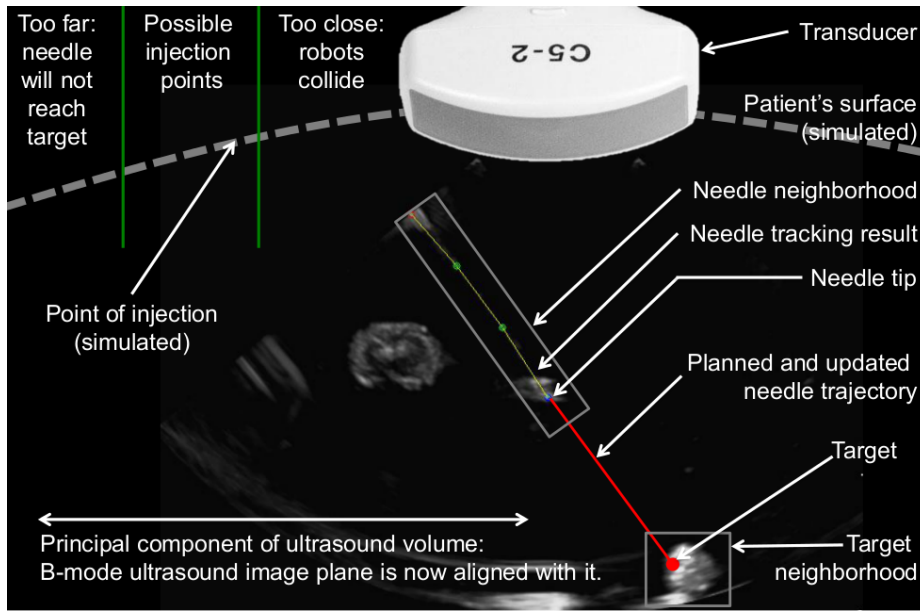


Fig. 3: While one robot holds the ultrasound transducer, the second robot injects the needle. The point of injection is computed by intersecting the image plane with the patient's surface. Additional constraints arise from collision avoidance and needle length. Needle tracking (yellow line) within the needle neighborhood (diagonal gray rectangular), as well as target tracking (red circle) under consideration of the target neighborhood (gray square) are explained in Sec. 2.4. The adaptive planned needle trajectory is visualized in red.

same image plane. For safety reasons, the needle is only allowed to traverse tissue that has already been imaged during the ultrasound volume acquisition, allowing the avoidance of critical anatomical structures.

We first compute the imaging plane, which is defined by the patient's surface, the target and the principal component of the ultrasound volume. This reduces the free configuration of the second robot, as the needle injection point now needs to be along a curve defined by the intersection of the image plane and patient's surface (see Fig. 3), but the needle trajectory inside the patient needs to be as short as possible, which limits the damage inflicted to the tissue and minimized the possibility of needle bending. By solving the kinematics of the robots under consideration of collision avoidance and minimal safety distances, the needle injection point is determined.

The determined needle trajectory is visualized within the previously acquired ultrasound volume. After the confirmation by the physician, the procedure is executed under visual servoing. The visual servoing considers the in-plane movements of the target and needle.

**Target tracking for visual servoing:** The visual error is directly determined by performing intensity-based registration of ultrasound images. First, an initial target neighborhood  $\Omega_0$  is defined based on the region of interest, which was

previously transferred from diagnostic imaging to the ultrasound image (Sec. 2.3). To guarantee sufficient overlap for intensity-based registration, while minimizing the computational effort, the size of the target neighborhood is suggested to be approximately 10% of the image width. The initial target neighborhood  $\Omega_0$  is confirmed by the users.

Then, the movement of the target neighborhood can be determined frame-to-frame by registration of the neighborhood  $\Omega_{t-1}$  to the current ultrasound image  $I_t$  using NCC as similarity measure and BOBYQA as optimizer. Because the deformation between two frames is assumed to be very small, a rigid transformation can be used. The neighborhood  $\Omega_t$  is used as an implicit mask during similarity computation.

In terms of target tracking, we are interested in the position of the target relative to the ultrasound apex which corresponds to the TCP. Knowing the original pose of the target at  $t = 0$ , the result can be described as transformation  ${}^{\text{US}}\mathbf{T}_{\text{Target}}$  which represents the position of the target in the current image  $I_t$  relative to the ultrasound origin (US).

**Needle tracking for visual servoing:** The needle appears in the image as a thin, high-intensity line, which is possibly curved. The point of needle injection and planned trajectory are known, and the point and time of entrance into the ultrasound image can easily be estimated. Furthermore, speed and approximate trajectory of the needle are known, which allows the reduction of the search space to a region which we will refer to as needle neighborhood  $\Theta$ .

Using a RANSAC-based approach with Kalman filtering [20], the needle can be detected and tracked in real-time. At each time  $t$ , the changes in  $\Theta$  are determined by simple subtraction  $\Delta\Theta_t = |\Theta_t - \Theta_{t-1}|$ . A set of candidate pixels are detected by thresholding using Otsu's method [21]:  $W_t = \{w_{i,t} \in \Theta_t | \Delta\Theta_t \geq T_{\text{Otsu},t}\}$ . Later, artifacts from ultrasound speckles are removed using a median filter, resulting in a reduced candidate set  $\hat{W}_t$ . Usually, it is a crucial part of needle tracking to determine whether or not the needle has moved. However, as the motion of the needle at the robot end-effector is known, we do not need to distinguish between frames with and without movement based on the intensity values.

At each time  $t$ , the needle is modeled by a polynomial curve  $C_t$  of degree  $n$  with  $n$  control points  $P_t = \{p_{m,t} | p_{m,t} = [x_{m,t}, y_{m,t}, z_{m,t}]\}_{m=1}^n$ . The  $k$  polynomial curves are fit to the reduced candidate set  $\hat{W}_t$  using the RANSAC algorithm [22], and the best fit is determined by computing the distance between the points in the candidate set and the polynomial curve. This distance is approximated by fitting a straight line to the control points  $P_t$ , projecting each candidate  $w_{i,t}$  and control point  $p_{m,t}$  onto the straight line, and using the ratios of distances between projected control points and projected candidates to approximate the closest point for each candidate on polynomial curve.

Using an extended Kalman filter [23], the update of the control points is performed based on the tracking information provided by the robot performing the needle injection and the needle tracking algorithm. This filtering step significantly improves the localization stability, and results in a transformation from the observed needle tip (oNT) to the ultrasound origin  ${}^{\text{US}}\mathbf{T}_{\text{oNT}}$ . Finally, the visual error between expected (based on mechanical tracking) and observed (based on RANSAC and Kalman filter) can be computed:

$${}^{\text{oNT}}\mathbf{T}_{\text{NT}} = {}^{\text{US}}\mathbf{T}_{\text{oNT}}^{-1} {}^{\text{US}}\mathbf{T}_{\text{F1}} {}^{\text{F1}}\mathbf{T}_{\text{B1}} {}^{\text{B2}}\mathbf{T}_{\text{B1}}^{-1} {}^{\text{F2}}\mathbf{T}_{\text{B2}}^{-1} {}^{\text{NT}}\mathbf{T}_{\text{F2}}^{-1}. \quad (3)$$

**Visual Control Law and Needle Trajectory Update:** The visual control law now determines the new needle trajectory under consideration of the transformations provided by the robot holding the ultrasound transducer  ${}^{F1}\mathbf{T}_{B1}$  (constantly updated as movement is possible while it remains in impedance control mode), the target tracking algorithm  ${}^{US}\mathbf{T}_{\text{Target}}$ , and the needle tracking algorithm  ${}^{oNT}\mathbf{T}_{NT}$ . The TCP pose (the needle tip and orientation) can now be updated according to:

$${}^{NT}\mathbf{T}_{F2} {}^{F2}\mathbf{T}_{B2} = {}^{oNT}\mathbf{T}_{NT} {}^{US}\mathbf{T}_{\text{Target}}^{-1} {}^{US}\mathbf{T}_{F1} {}^{F1}\mathbf{T}_{B1} {}^{B2}\mathbf{T}_{B1}^{-1}. \quad (4)$$

Target tracking and needle detection are continuously executed, allowing the visual servoing to be performed in near real-time. All trajectories are generated using cubic polynomials with via-points. The maximum force applied is set to 5 Newton.

### 3 EXPERIMENTS and RESULTS

#### 3.1 Experimental Setup

For both intraoperative and preoperative imaging, we use an ultrasonix® SonixTable™ system together with a curvilinear transducer C5-2/60 is used to obtain the ultrasound images (Ultrasonix Medical Corp., Richmond, BC, Canada). The acquisition rate, frequency, depth and gain are set to 32 Hz, 5.0 MHz, 90 mm, and to 32%, respectively. Using the Ultrasonix® API, the images are transferred via ethernet. The needle is a standard 18 gauge needle for seed placement. The RGB-D camera is an Intel® RealSense™ F200 3D camera, which provides a RGB data at  $1920 \times 1080$  pixels at 30 frames per second and depth images at a resolution of  $640 \times 480$  pixels at 60 frames per second. The observable depth range is 0.2 to 1.2 meters. To mount the ultrasound transducer, needle and RGB-D cameras to the robots, custom adapters were designed and 3D printed. For experiments we use two identical KUKA LBR Intelligent Industrial Work Assistant (iiwa) 7 R800 robots (KUKA Roboter GmbH, Augsburg, Germany). Each robotic system is comprised of a 7 joint arm with corresponding control units and consequently enables one redundant degree of freedom (7 in total). As a result of this design, the robot provides dynamic movement and flexible adaption of trajectories to the working environment. With respect to robotic ultrasound, the incorporated high-accuracy torque sensors in every of the seven joints are evenly important, as a robotic ultrasound platform has to be fully compliant to both patient and staff. Detailed specifications can be found in [24]. The experimental setup is shown in Fig. 4.

#### 3.2 Implementation Details

The image processing computer runs the ImFusion Suite (ImFusion GmbH, Munich, Germany) for which we have designed and implemented additional modules to acquire the RGB-D point clouds, allow user interaction, trajectory planning and real-time ultrasound visualization. All modules and algorithms are implemented to be parallelized using the GPU, which allows fast and efficient processing of all system components.

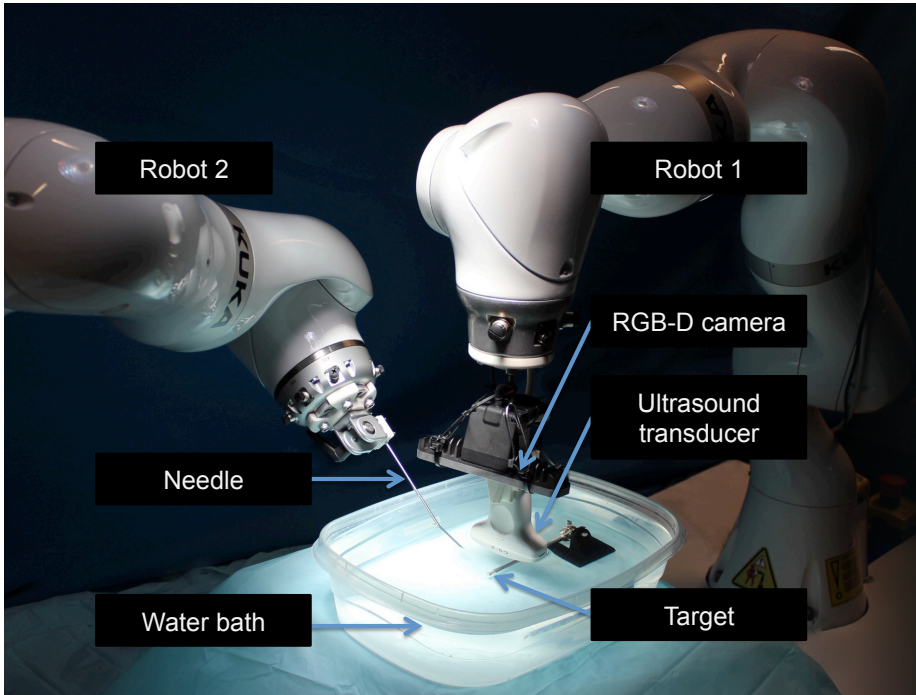


Fig. 4: The experimental setup is comprised by two KUKA iiwa, holding the needle and ultrasound transducer. After calibration of the base-to-base transformation, visual servoing can be performed in order to place the needle in the target, which is observed in the ultrasound image.

The Fast Research Interface (FRI) allows the full low-level real-time control of the KUKA iiwa via UDP at rates up to 1 kHz [25]. The latest version of the FRI for the KUKA iiwa allows the monitoring of the robot joint positions, but provides no feedback on the Euclidean pose. Utilizing the V-REP model, we can solve the forward kinematics and obtain the Euclidean positions at a rate of 250 Hz, which outperforms any commonly used clinical tracking system.

The robots are controlled by a driver software using the KUKA SmartServo. Command messages are sent from the image processing computer via CAMP RoboLib, which uses an OpenIGTLink connection. KUKA SmartServo can currently process commands at a rate of 50 Hz.

### 3.3 Needle Placement Experiments and Results

The spatial transformation  ${}^{\text{US}}\mathbf{T}_{\text{F1}}$  from the origin of the ultrasound image to the transducer apex is preliminary determined by using publicly available PLUS library 2.2.0 [26] and a 3D printed calibration phantom. The mean calibration error is  $0.56 \pm 0.20$  mm.

We then performed two sets of experiments, using two different types of phantoms. The first type of phantom is a 260x19x135 mm box filled with water. The

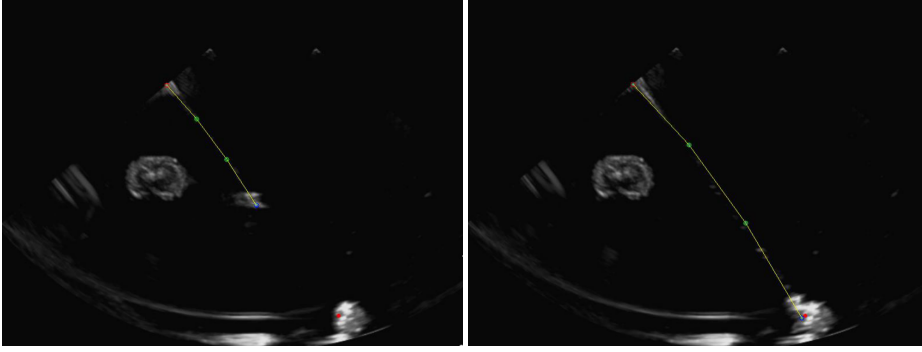


Fig. 5: Different instances of the needle tracking while approaching a target. The yellow line represents the fitted polynomial, blue circle is the tracked tip and the full red circle is the user selected target.

Table 1: Average distances between needle tip and targets for experiments with visual servoing. Each line summarizes five experiments.

#	Phantom Type	Angle	Avg. Errors 5mm/s [mm]	Avg. Errors 3mm/s [mm]	Avg. Errors 1mm/s [mm]
1	Water	30°	1.19 ± 0.12	1.30 ± 0.16	1.29 ± 0.09
2	Water	45°	1.14 ± 0.09	1.07 ± 0.14	0.90 ± 0.11
3	Gel	30°	0.87 ± 0.16	0.97 ± 0.15	0.82 ± 0.12
4	Gel	45°	0.87 ± 0.14	0.93 ± 0.20	0.81 ± 0.19

target is a 7 mm sphere which is submerged around 80 mm below the surface. A water bath allows easy ultrasound imaging, but the impedance controller cannot be used. The other phantom is made by filling a 240x150x120 mm box with 7 weight percent(wt%) gelatin. Different organic sphere like objects ranging from around 17 mm to 7 mm were then submerged at different depths below the surface. For our tracking accuracy experiments we again used a 7 mm sphere which was around 80 mm below the surface. During the gelatin phantom tests, all movements are executed using the impedance controller. For each phantom we have performed needle insertion with two different angles, 45° and 30° with respect to the base plane of the box, and three different needle insertion velocities: 5 mm/s, 3 mm/s and 1 mm/s. The needle insertion has been performed five times in each test case, resulting in a total of 60 evaluated needle insertions. Higher and lower needle insertion angles were not considered to avoid a collision between the two robots and between one robot and the phantom.

We evaluated the needle tracking algorithm by recording the detected needle tip at different instances of time, as shown in Fig. 5. When the robot reaches the planned end point of the trajectory we calculate the distance between the detected needle tip and the desired target position in the Ultrasound image. Due to the known calibration between the US image and the robot flange we are also able to compute the metric error. The results are summarized in Tab. 1.

## 4 DISCUSSION and CONCLUSION

In this work, we closed the planning-imaging-action loop, and presented a framework for robotic needle placement under robotic ultrasound image guidance. In particular, we demonstrated for the first time the use of a dual-robot system that takes advantage of impedance control for ultrasound imaging and allows for a consistent representation of the workspace. Our platform encompasses state of the art ultrasound image compounding techniques for representing the targeted domain, as well as needle tracking techniques suitable for real time operation. Once integrated the platform, we demonstrated needle placement in a simplified setting using two different types of phantoms (water and gel). We obtained order of 1 mm targeting accuracy when considering a target point submerged in the above phantoms, irrespective of the needle orientation and speed. This supports the suitability of the proposed approach in a range of operating conditions, even if further characterization is needed to properly map the platform performance. For instance, we need to consider physically representative tissue (e.g. soft biological tissues) for which ultrasound imaging might pose further challenges. Moreover, in a more realistic scenario, flexible needle deformation in soft tissue should be also considered. Nonetheless, while laying no claims of generality, our results demonstrate that we effectively closed planning-imaging-action loop. Let us remark that our approach is quite general, so that it can be also applied to platform encompassing different robotic components. We plan to extend this work by framing the proposed approach in a more clinically relevant environment. In particular, we will properly integrate preoperative imaging by using CT or MRI techniques, as applied to a relevant interventional test case like needle placement in the spine, or within organs in the abdominal cavity. This way, our workflow could be further defined based on interventional constraints, paving the way for the effective use of the proposed dual-robot ultrasound-guided interventional platform.

## ACKNOWLEDGEMENT

The authors wish to thank Wolfgang Wein and his team (ImFusion GmbH, Munich, Germany) for the great support and opportunity use the ImFusion framework.

## References

1. N. Abolhassani, R. Patel, and M. Moallem, "Needle insertion into soft tissue: A survey," *Medical Engineering & Physics*, vol. 29, no. 4, pp. 413 – 431, 2007.
2. J. Hong, T. Dohi, M. Hashizume, K. Konishi, and N. Hata, "An ultrasound-driven needle-insertion robot for percutaneous cholecystostomy," *Physics in Medicine and Biology*, vol. 49, no. 3, p. 441, 2004.
3. Z. Wei, M. Ding, D. Downey, and A. Fenster, "3d trus guided robot assisted prostate brachytherapy," in *Medical Image Computing and Computer-Assisted Intervention—MICCAI 2005*. Springer, 2005, pp. 17–24.
4. S. P. DiMaio and S. Salcudean, "Needle steering and motion planning in soft tissues," *Biomedical Engineering, IEEE Transactions on*, vol. 52, no. 6, pp. 965–974, 2005.
5. R. Alterovitz, K. Goldberg, and A. Okamura, "Planning for steerable bevel-tip needle insertion through 2d soft tissue with obstacles," in *Robotics and Automation, 2005. ICRA 2005. Proceedings of the 2005 IEEE International Conference on*. IEEE, 2005, pp. 1640–1645.

6. M. Abayazid, G. J. Vrooijink, S. Patil, R. Alterovitz, and S. Misra, "Experimental evaluation of ultrasound-guided 3D needle steering in biological tissue," *International journal of computer assisted radiology and surgery*, vol. 9, no. 6, pp. 931–939, 2014.
7. P. Chatelain, A. Krupa, and N. Navab, "3D ultrasound-guided robotic steering of a flexible needle via visual servoing," in *IEEE Int. Conf. on Robotics and Automation, ICRA '15*.
8. A. Ahmad, M. Cavusoglu, and O. Bebek, "Calibration of 2D Ultrasound in 3D space for Robotic biopsies," in *Advanced Robotics (ICAR), 2015 International Conference on*, July 2015, pp. 40–46.
9. M. Niccolini, V. Castelli, C. Diversi, B. Kang, F. Mussa, and E. Sinibaldi, "Development and preliminary assessment of a robotic platform for neuroendoscopy based on a lightweight robot," *The International Journal of Medical Robotics and Computer Assisted Surgery*, 2015.
10. Y. C. Shiu and S. Ahmad, "Calibration of wrist-mounted robotic sensors by solving homogeneous transform equations of the form  $AX=XB$ ," *Robotics and Automation, IEEE Transactions on*, vol. 5, no. 1, pp. 16–29, Feb 1989.
11. Z. Zhang, "A flexible new technique for camera calibration," *Pattern Analysis and Machine Intelligence, IEEE Transactions on*, vol. 22, no. 11, pp. 1330–1334, 2000.
12. L. Mercier, T. Langø, F. Lindseth, and L. D. Collins, "A review of calibration techniques for freehand 3-d ultrasound systems," *Ultrasound in medicine & biology*, vol. 31, no. 2, pp. 143–165, 2005.
13. A. Albu-Schäffer, C. Ott, U. Frese, and G. Hirzinger, "Cartesian impedance control of redundant robots: Recent results with the DLR-Light-Weight-arms," in *Robotics and Automation, 2003. Proceedings. ICRA '03. IEEE International Conference on*, vol. 3. IEEE, 2003, pp. 3704–3709.
14. R. B. Rusu, Z. C. Marton, N. Blodow, M. Dolha, and M. Beetz, "Towards 3D point cloud based object maps for household environments," *Robotics and Autonomous Systems*, vol. 56, no. 11, pp. 927–941, 2008.
15. A. Karamalis, W. Wein, O. Kutter, and N. Navab, "Fast hybrid freehand ultrasound volume reconstruction," in *SPIE Medical Imaging*. International Society for Optics and Photonics, 2009, pp. 726 114–726 114.
16. L. G. Brown, "A survey of image registration techniques," *ACM computing surveys (CSUR)*, vol. 24, no. 4, pp. 325–376, 1992.
17. B. Fuerst, W. Wein, M. Müller, and N. Navab, "Automatic ultrasound–MRI registration for neurosurgery using the 2D and 3D LC2 metric," *Medical image analysis*, vol. 18, no. 8, pp. 1312–1319, 2014.
18. W. Wein, S. Brunke, A. Khamene, M. R. Callstrom, and N. Navab, "Automatic CT-ultrasound registration for diagnostic imaging and image-guided intervention," *Medical image analysis*, vol. 12, no. 5, pp. 577–585, 2008.
19. M. J. Powell, "The BOBYQA algorithm for bound constrained optimization without derivatives," 2009.
20. P. Chatelain, A. Krupa, and M. Marchal, "Real-time needle detection and tracking using a visually servoed 3d ultrasound probe," in *Robotics and Automation (ICRA), 2013 IEEE International Conference on*. IEEE, 2013, pp. 1676–1681.
21. N. Otsu, "A threshold selection method from gray-level histograms," *Automatica*, vol. 11, no. 285–296, pp. 23–27, 1975.
22. M. Uherčík, H. Liebgott, J. Kybic, and C. Cachard, "Needle localization methods in 3D ultrasound data," in *International Congress on Ultrasonics*, 2009, pp. 11–17.
23. S. Julier and J. Uhlmann, "Unscented filtering and nonlinear estimation," *Proceedings of the IEEE*, vol. 92, no. 3, pp. 401–422, Mar 2004.
24. R. Bischoff, J. Kurth, G. Schreiber, R. Koeppe, A. Albu-Schäffer, A. Beyer, O. Eiberger, S. Haddadin, A. Stemmer, G. Grunwald *et al.*, "The KUKA-DLR Lightweight Robot arm—a new reference platform for robotics research and manufacturing," in *Robotics (ISR), 2010 41st international symposium on and 2010 6th German conference on robotics (ROBOTIK)*. VDE, 2010, pp. 1–8.
25. G. Schreiber, A. Stemmer, and R. Bischoff, "The Fast Research Interface for the KUKA Lightweight Robot," in *IEEE Workshop on Innovative Robot Control Architectures for Demanding (Research) Applications How to Modify and Enhance Commercial Controllers (ICRA 2010)*, 2010.
26. A. Lasso, T. Heffter, A. Rankin, C. Pinter, T. Ungi, and G. Fichtinger, "Plus: Open-source toolkit for ultrasound-guided intervention systems," *IEEE Transactions on Biomedical Engineering*, no. 10, pp. 2527–2537, Oct 2014. [Online]. Available: <http://perk.cs.queensu.ca/contents/plus-open-source-toolkit-ultrasound-guided-intervention-systems>